A novel layered reconstruction framework for longitudinal segmented electromagnetic calorimeter*

Jia-Le Fei,[1] Ao Yuan,[1] Ke Wei,[2] Liang Sun,[2,†] and Ji-Ke Wang[1,‡]

[1]*The Institute for Advanced Studies, Wuhan University, Wuhan 430072, China*
[2]*School of Physics and Technology, Wuhan University, Wuhan 430072, China*

In future high-energy physics experiments, the electromagnetic calorimeter (ECAL) will operate in exceptionally high-luminosity. An ECAL featuring layered readout in the longitudinal direction and precise time-stamped information offers a multi-dimensional view, enriching our comprehension of the showering process of electromagnetic particles in high-luminosity environments. And it is taken as the baseline design for several new experiments, including the planned upgrades of the current running experiments. Reconstructing and matching the multi-dimensional information across different layers poses new challenges in utilizing layered data effectively. This work introduces a novel layered reconstruction framework for the ECAL with a layered readout information structure and develops the layered clustering algorithm. It expands the concept of clusters from planes to multiple layers. Additionally, this work presents the corresponding layered cluster correction methods, investigates the transverse shower profile, which is utilized for overlapping clusters splitting, and develops the layered merged π^0 reconstruction algorithm based on this framework. By incorporating energy and time information in 3-dimension, this framework provides a suitable software platform for the preliminary research of longitudinal segmented ECAL and new perspectives in physics analysis.

Furthermore, taking the PicoCal in LHCb Upgrade II as a concrete example, the performance of the framework has been preliminarily evaluated using single photons and π^0 particles from the neutral B^0 meson decay $B^0 \to \pi^+\pi^-\pi^0$ as benchmarks. The results demonstrate that compared to the unlayered framework, utilizing this framework for longitudinal segmented ECAL significantly enhances the position resolution and the ability to split overlapping clusters, thereby improving the reconstruction resolution and efficiency for photons and π^0s.

Keywords: Electromagnetic calorimeter. Layered reconstruction. Transverse shower profile. Merged π^0 reconstruction.

I. INTRODUCTION

Electromagnetic calorimeter (ECAL) is a detector used to measure the energy and momentum of high-energy electromagnetic particles (e.g., electrons, photons, etc.). In particle physics, ECAL is able to measure the electromagnetic showering of particles within it and determines the energy and momentum information of electromagnetic particles based on the energy deposition, providing important information for understanding the properties and interactions of elementary particles.

A high-performance ECAL is crucial for the precise detection of high-energy physical phenomena and has been validated in many experiments[1–4]. For instance, in the context of the LHCb experiment, during Run 1 and Run 2 of the Large Hadron Collider (LHC), approximately 33% of the decay products of heavy flavor particles are neutral particles, which decay to photons, such as π^0[5]. These photons exhibit a broad energy spectrum, ranging from a few GeV to several hundred GeV[6]. And thanks to the outstanding performance of the ECAL in LHCb[7, 8], the Run 1 and Run 2 experiments yielded a lot of impactful researches involving photons, π^0s and electrons. The researches covered the exploration of photon polarization in the $b \to s\gamma$ process[9], radiative B_s^0 decays[10], and other related studies. Additionally, the quantification of CP violation in decays such as $B^+ \to K^+\pi^0$ decays[11] and $D^0 \to \pi^+\pi^-\pi^0$ decays[12] were conducted. Furthermore, intriguing investigations into lepton universality through the reconstruction of $b \to s\ell^+\ell^-$ transitions were performed[13][14]. The research also included rare decay searches, such as $B_s^0 \to \mu^+\mu^-\gamma$[15], among others.

In the pursuit of new physics at the LHC, the high-luminosity LHC (HL-LHC) project has been proposed to enhance the accumulation of collision data within a shorter timeframe [16–18]. Operating with an instantaneous luminosity reaching 10^{34} $\mathrm{cm}^{-2}\mathrm{s}^{-1}$, the HL-LHC aims to amass an impressive integrated luminosity over its operational lifetime [17, 19]. However, such high luminosity environment presents challenges such as increased detector occupancy, vertex pile-ups, and radiation resistance concerns. Many current detectors at the LHC are no longer adequate for operation at HL-LHC condition, and also due to the long term radiation damage, necessitating urgent replacements. To ensure optimal detector performance in high luminosity settings and facilitate new physics exploration, several experiments are planning detector upgrades [20–24].

The showering process of electromagnetic particles in an ECAL is influenced by factors such as particle type and incident energy, which, in turn, affect the distribution of deposited energy [25]. An ECAL equipped with multiple readout channels, spanning both transverse and longitudinal directions, facilitates the capture of time, energy, and other readout data in dual dimensions. This capability significantly enhances our comprehension of the physical processes within the ECAL across multiple dimensions, ultimately leading to improved accuracy in reconstructing the energy and momentum of particles. Therefore, the longitudinal segmented ECAL has been taken as a baseline design in upgrades for many experiments.

The development of event reconstruction algorithms that

*

† Corresponding author, E-mail address: liang.sun@cern.ch
‡ Corresponding author, E-mail address: Jike.Wang@cern.ch

fully exploit the energy, position, and time information acquired from the longitudinally segmented ECAL will enhance the precision of energy-momentum reconstruction, cluster splitting, and particle identification, thereby facilitating the achievement of defined physical objectives. However, this also introduces new challenges in how to reconstruct, match, and efficiently utilize the longitudinal layer information. To leverage the advantages of layered readouts, in forthcoming high-energy physics experiments such as CMS, ALICE, etc. [26–29], diverse software frameworks and reconstruction algorithms have been devised and customized to effectively utilize and store layered information.

Building upon the aforementioned background, this work presents a comprehensive software framework tailored for a longitudinally segmented ECAL, along with the development of a layered clustering algorithm and cluster correction workflow. The layered reconstruction framework outlined in this research merges data from the all layers to pinpoint potential $Cluster^{3D}$ candidates. Subsequently, a seed will be identified in each layer from the readout cells of these $Cluster^{3D}$ candidates. Utilizing these seeds as focal points, $Cluster^{2D}$s in the all readout layers will be reconstructed (The definitions of $Cluster^{3D}$ and $Cluster^{2D}$ will be elaborated in the subsequent sections). Finally, the performance is compared with an unlayered reconstruction algorithm that simply combines the information from corresponding readout units in each layer, based on single-photon resolution, as well as the reconstruction resolution and efficiency for π^0 from $B^0 \to \pi^+\pi^-\pi^0$. The comparison leverages the 2023 baseline setup of ECAL in LHCb Upgrade II (PicoCal)[30, 31].

II. SOFTWARE FRAMEWORK AND DATA STRUCTURES

The layered reconstruction framework is shown in the Fig. 1. Modelling of the detector geometry is the cornerstone of the framework. In order to adapt as many longitudinally segmented ECAL structures as possible, the following data structures are constructed to describe and carry the geometrical information of the ECAL in this framework.

Calorimeter: It represents the ECAL and also stores the absolute coordinates and size of the entire ECAL in space.

Region: It is a virtual geometry containing a series of **modules** with identical detector structure, material, and installation angle. And it is used to store the calibration and cluster correction parameters for this series of **modules**.

Module: It represents the minimum installation unit and stores the absolute coordinates, size and installation angle of itself.

Layer: It is the key geometric data structure in this framework, and physically represents a longitudinal segment of the **module**. It stores all **Cell$^{\mathbf{2D}}$**s that are located at a segmented readout layer in a **module**.

Cell$^{\mathbf{2D}}$: It represents the minimum readout channels in modules and contains information about the mounting position of the readout cell, the readout signal, and the readout time-stamp.

Based on the aforementioned basic geometry structure, the following cluster data structures containing two or more $Cell^{2D}$s are constructed and corresponding to the cluster layer in the software framework. And the specific construction method of the following data structures will be introduced in Sec. III A.

Cell$^{\mathbf{3D}}$: It consists of multiple $Cell^{2D}$s in the longitudinal direction.

Cluster$^{\mathbf{2D}}$: It consists of multiple $Cell^{2D}$s at the same layer.

Cluster$^{\mathbf{3D}}$: It consists of a $Cluster^{2D}$ and multiple $Cell^{2D}$s in each layer and would be considered as a candidate for photons, electrons, or merged π^0s.

III. RECONSTRUCTION

Based on the layered reconstruction framework, this section will detail the reconstruction algorithm of the $Cluster^{3D}$, which serve as the candidates for electromagnetic particles (γ/e). And it will also discuss the methodology for reconstructing a merged π^0 by splitting a single $Cluster^{3D}$. Additionally, it will outline the process for correcting various parameters of the $Cluster^{3D}$, including energy, position, and time.

A. Layered clustering

The algorithm outlined in this section will detail the methodology to finalize the construction of $Cluster^{3D}$s and providing particle reconstruction information at each readout layer in the form of $Cluster^{2D}$s. The flowchart of the layered clustering algorithm is shown in Fig. 2d. Firstly, the algorithm search for $Seed^{3D}$s on a single layer, which includes the realistic readout layer with smaller transverse showering width, as well as a virtual single-layer calorimeter constructed by merging information from all readout layers and construct temporary $Cluster^{3D}$s in the virtual single-layer calorimeter from $Seed^{3D}$s. This approach is motivated by two primary considerations.

The first and most important point is that constructing $Cluster^{2D}$ in each layer and performing layer-by-layer matching will consume a significant amount of computational time. First, performing 2-dimension clustering in single layer will ensure efficient online triggering.

Secondly, in layers with narrower transverse cluster development, there is a chance to discover more non-overlapping clusters, but at the same time, due to the narrower transverse cluster development, there is less energy deposition. Because

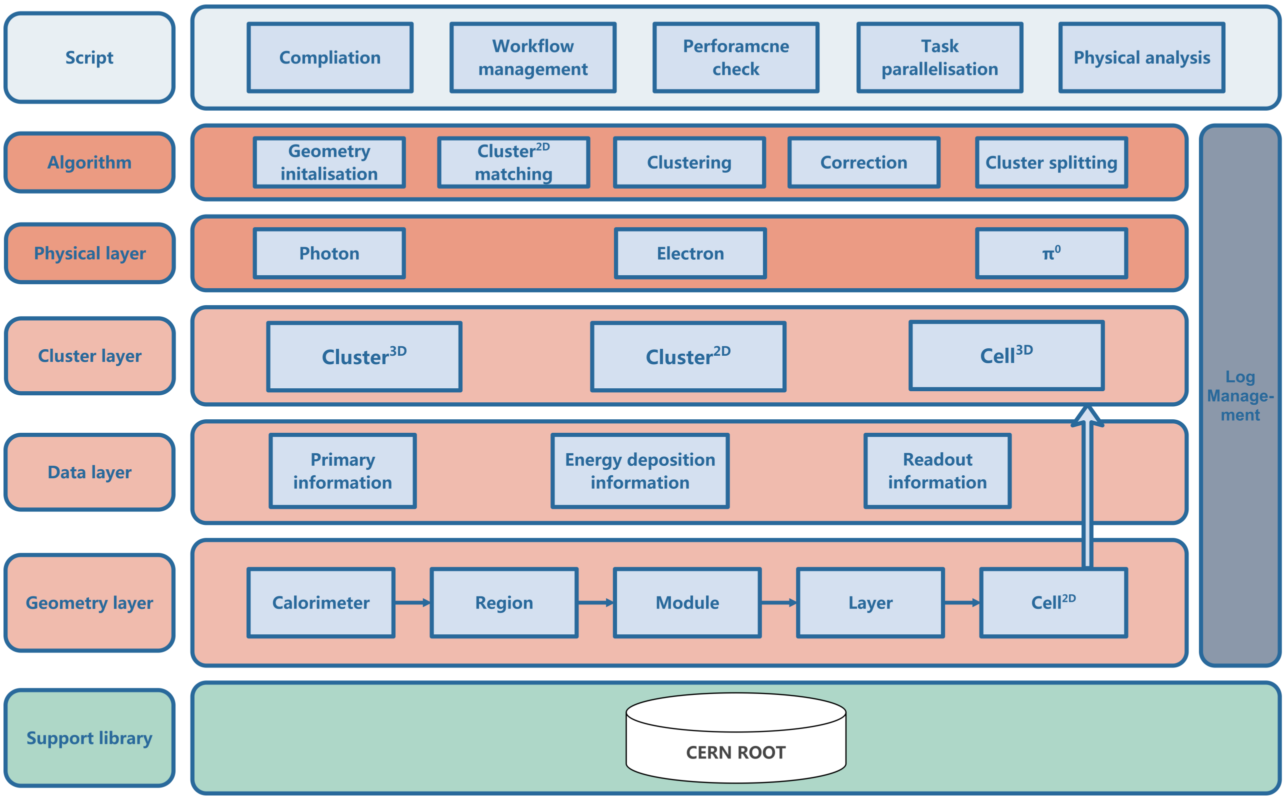

Fig. 1. Software framework.

of sampling fluctuations, some particles may not form effective seeds in this layer. Therefore, searching for $Seed^{3D}$s from both $Cell^{3D}$s and $Cell^{2D}$s in layers with narrower cluster development will help us achieve a balance in cluster separation and reconstruction efficiency.

Subsequently, based on the temporary $Cluster^{3D}$s, construct $Cluster^{2D}$s located on different layers to obtain the final $Cluster^{3D}$s. The integration of information from the different layers is initially performed by constructing a $Cell^{3D}$. Details about each step of the layered clustering algorithm will be elaborated in the following:

1. Constructing $Cell^{3D}$

To integrate the information in each readout layer, the information from the corresponding $Cell^{2D}$s on both layers is utilized to establish a novel data structure known as $Cell^{3D}$. Specifically, the $Cell^{3D}$s are systematically constructed across the transverse section of the ECAL with a radius size equivalent to the module's Molière radius. Along the longitudinal direction of the ECAL, all $Cell^{2D}$s falling within the transverse span of a $Cell^{3D}$ are amalgamated into this $Cell^{3D}$, with each $Cell^{2D}$ being included only once. The energy of the $Cell^{3D}$ is determined by the cumulative energies of the $Cell^{2D}$s it encompasses, and the position of the $Cell^{3D}$ is defined as its geometric centre.

2. Searching $Seed^{3D}$ and constructing temporary $Cluster^{3D}$

When an electromagnetic particle strikes the ECAL, it will radiate energy outward from the impact point, typically resulting in the formation of the $Cell^{2D}$ and $Cell^{3D}$ with the highest local energy deposition near the impact point. Therefore, as depicted in Fig. 2a, the initial step in clustering is to iterate through all $Cell^{3D}$s and $Cell^{2D}$s in specific layers to identify the $Cell^{3D}$ and $Cell^{2D}$ exhibiting the highest local energy deposition. For the local maximum $Cell^{2D}$, the corresponding $Cell^{3D}$ will be considered as a $Seed^{3D}$. At the same time, the local maximum $Cell^{3D}$ will also be considered as a $Seed^{3D}$. The *seed* indicates that it serves as the initial of the clustering process.

To prevent the faker $Seed^{3D}$s during the seeding process, all identified $Seed^{3D}$ must satisfy a transverse momentum cut, typically defined to be greater than 50 MeV in this framework. The threshold value of this cut can be lowered if required for investigating phenomena related to soft photons or electrons. All the $Seed^{3D}$s passing the cut are labelled as the final $Seed^{3D}$s and stored.

As a result of the transverse particle showering, the energy is not fully contained within $Seed^{3D}$. Hence, it is imperative to encompass a specific range of $Cell^{3D}$s around $Seed^{3D}$ to guarantee optimal coverage of all energy deposits from the particles. In this work, we will follow the method described in Ref. [32] which uses a window of fixed size to incorporate $Cell^{3D}$s. The specific procedure is as follows:

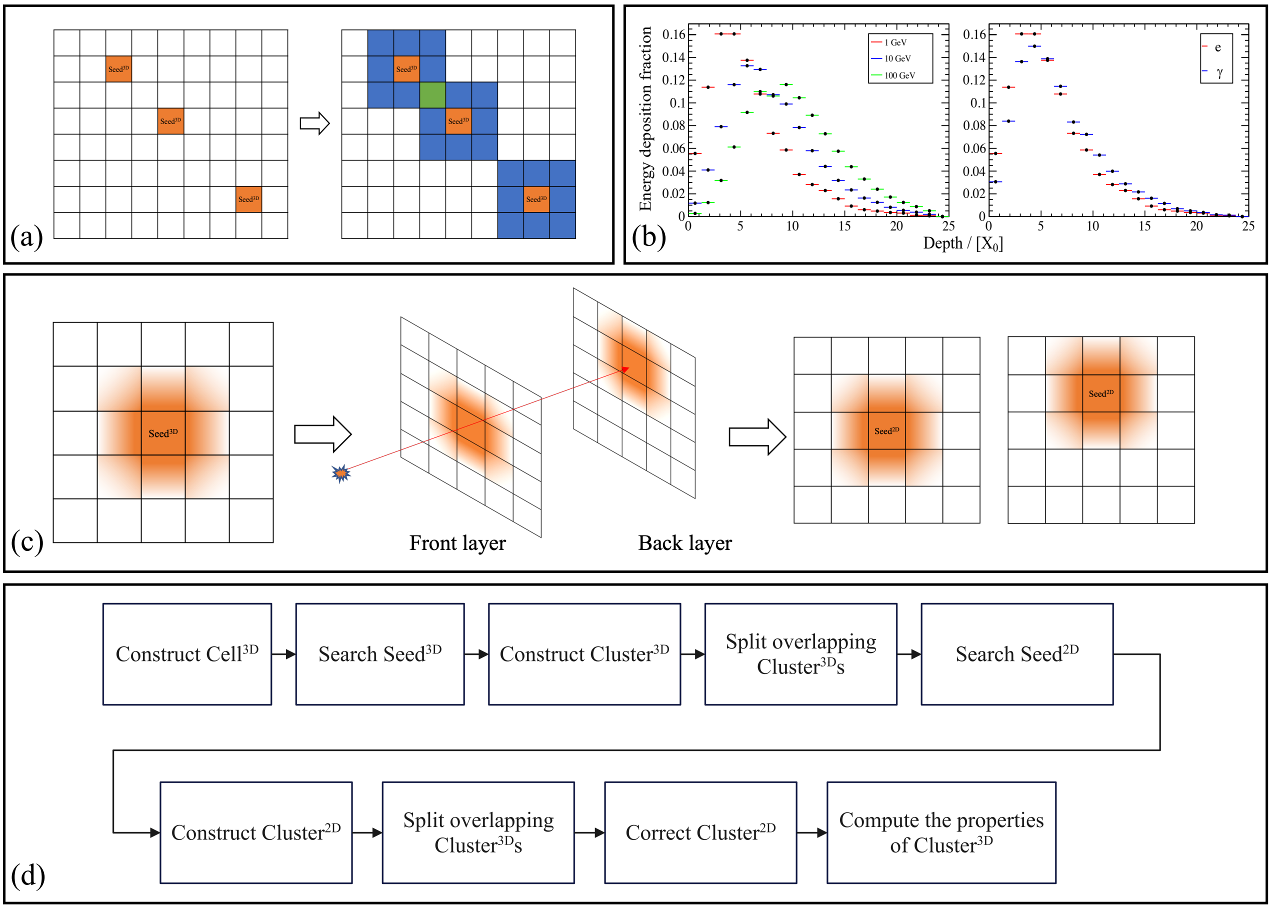

Fig. 2. (a): Searching $Seed^{3D}$s and constructing temporary $Cluster^{3D}$s centred on $Seed^{3D}$s, where the orange boxes represent $Seed^{3D}$s, the blue boxes represent $Cell^{3D}$s, and the green box represents $Cell^{3D}$ shared by two $Cluster^{3D}$s. (b): The energy deposition in the longitudinal direction of ECAL, where the left plot shows electrons with different energies and the right plot shows the electron and photon with 1 GeV energy. (c): Searching $Seed^{2D}$ in the $Cell^{2D}$ of the temporary $Cluster^{3D}$ and constructing new $Cluster^{2D}$ in each layer. (d): Work flow chart for layered reconstruction.

centred around the $Seed^{3D}$s, the $Cluster^{3D}$s are formed by incorporating all $Cell^{3D}$s within a 3×3 window around the $Seed^{3D}$s, as illustrated in Fig. 2a. Additionally, the $Cell^{2D}$s from all layers encompassed by the $Cell^{3D}$s are also included as member of the $Cluster^{3D}$s. However, when the $Seed^{3D}$ is located at the boundary of region, a special treatment is required due to the different types of $Cell^{3D}$s in different regions. Around the $Seed^{3D}$, within a radius of 1.5 times the size of the $Seed^{3D}$, $Cell^{3D}$s belonging to other regions will also be included. In this paper a more detailed process is not described. The above process may lead to the $Cluster^{3D}$ at the boundary containing a number of $Cell^{3D}$s that may be greater or less than 9, and its shape may not be regular. This requires separate handling of the $Cluster^{3D}$ at the boundary in the $Cluster^{3D}$ correction process described later in the paper.

In subsequent steps, further layered modifications will be made to the $Cell^{2D}$s included in the $Cluster^{3D}$. Therefore, the $Cluster^{3D}$ obtained in this section are referred to as the temporary $Cluster^{3D}$.

3. *Searching $Seed^{2D}$ and reconstructing $Cluster^{2D}$*

Due to the incident angle of particles and the rotation of certain modules, as the shower evolves longitudinally, the energy centroid of the shower will vary across different layers. This results in the $Cell^{2D}$ with the highest local energy in each layer not always being encompassed within the $Seed^{3D}$, as depicted in Fig. 2c.

To identify the $Seed^{2D}$ in each layer, we will iterate through the $Cell^{2D}$s of each layer in the temporary $Cluster^{3D}$ and select the $Cell^{2D}$ with the highest energy as the $Seed^{2D}$ for that layer. Moreover, the overlap of $Cluster^{2D}$s will result in an increased accumulation of energy in shared $Cell^{2D}$s, which may cause the energy of a shared $Cell^{2D}$ to exceed that of the $Seed^{2D}$, leading to the misidentification of a shared $Cell^{2D}$ as a $Seed^{2D}$. Therefore, before searching for $Seed^{2D}$, energy splitting needs to be performed on all overlapping $Cluster^{2D}$s as shown in Fig. 2d, which will be discussed in detail in Sec. III B 3.

Subsequently, $Cluster^{2D}$s are formed with $Seed^{2D}$s as the centre, and all $Cell^{2D}$s within the Molière radius of the

module and centred on $Seed^{2D}$s in the same layer are included in the $Cluster^{2D}$s. The raw energy, position, and timestamp of the $Cluster^{2D}$s are computed using the following equations:

$$\begin{aligned} E_{raw} &= \sum_{i=1}^{n} E_i, \\ r_{raw} &= \frac{\sum_{i=1}^{n} E_i * r_i}{E_{raw}}; \quad r = x \ or \ y, \\ t_{raw} &= t_{Seed^{2D}}, \end{aligned} \tag{1}$$

where n represents the number of $Cell^{2D}$s in this $Cluster^{2D}$, and r_i and E_i represent the position and energy of the $Cell^{2D}$s.

Finally, a new $Cluster^{3D}$ which contains the $Cluster^{2D}$s in all layers is constructed. The raw energy of the $Cluster^{3D}$ is computed by the formula below:

$$E^{3D}_{raw} = \sum_{i=1}^{n} E_i, \tag{2}$$

where E_i also represents the energy of the $Cell^{2D}$s and n represents the number of the $Cell^{2D}$s in all layers incorporated in the $Cluster^{3D}$. As shown in Fig. 2b, the energy deposition distribution of incident particles is dependent on the type and energy of the incident particles. Therefore, the unreasonable $Cluster^{3D}$s can be filtered out based on the energy ratio of $Cluster^{2D}$s in each layer. The position information of $Cluster^{2D}$s is considered as a point of the incident particle momentum direction on the corresponding layer, with the time information serving as the timestamp for this coordinate point. Additionally, the energy information is regarded as the total deposited energy of the particle in that layer. Reconstructing and correcting the information of particles along the momentum direction layer by layer will help improve the position resolution, and this will be discussed in detail in Sec. IV.

B. $Cluster^{3D}$ correction

The goal of the $Cluster^{3D}$ correction is to reduce the bias between the reconstructed values and the actual values, while also aiming for the minimal standard deviation of the reconstructed values. In the layered reconstruction framework, the calculation and correction of the position and timestamp of $Cluster^{3D}$ will be carried out from the $Cluster^{2D}$ level firstly. As described in Sec. III A, the raw position and timestamp of the $Cluster^{2D}$ can be calculated using the information from the $Cell^{2D}$s in the $Cluster^{2D}$. After that, the raw position and timestamp information of the $Cluster^{2D}$ will be corrected, and then the position and timestamp information of $Cluster^{3D}$ will be calculated using the corrected $Cluster^{2D}$. The energy of $Cluster^{3D}$ will also be corrected using the energy ratios of the $Cluster^{2D}$s in different layers. To provide a more detailed illustration of the specifics in the layered corrections, Fig. 3 also displays some examples by the longitudinal segmented PicoCal in LHCb Upgrade II, where the $Front$ and $Back$ represent the front and back layers of the above-mentioned ECAL.

1. *Energy correction*

The objective of energy correction is to correct the energy of the $Cluster^{3D}$ to match that of the incident particle. Errors in reconstructing the energy of the incident particle typically stem from the following sources:

Intrinsic error of ECAL readout cell: It comes from the response linearity of sensitive materials, thermal noise in electronic systems, sampling errors in analogue to digital converters (ADC), etc.

Calibration error of the readout cell: The shower development in the longitudinal direction is energy related, and the proportion of physical processes dominated in energy deposition changes at different stages of shower development. This leads to changes in the sampling fraction of the ECAL, which ultimately affects the calibration of the readout cell.

Leakage of energy: It is due to the incomplete deposition of particle energy in ECAL and the use of finite-sized windows during clustering.

Fitting error of calibration and correction parameters: It is usually expressed as a constant term in the energy resolution.

In the layered framework of this work, the energy correction of $Cluster^{3D}$s is divided into two steps, as shown in Fig. 3a and Fig. 3b. The initial correction of the energy of $Cluster^{3D}$ is performed based on the energy ratio of $Cluster^{2D}$s in the different layers. As shown in Fig. 3a, in the example based on the PicoCal, we first correct the bias between the reconstructed $Cluster^{3D}$ energy and the true energy based on the energy ratio of the front layer to the back layer. Subsequently, as illustrated in Fig. 3b, further correction of the energy of $Cluster^{3D}$s is conducted based on the total energy of $Cluster^{3D}$s and it reduces the bias in the low energy region.

2. *Position and time correction*

When a particle passes through the ECAL, it showers and deposits energy along the direction of the particle momentum. The centre of gravity of the deposited energy in each layer can be considered as a point in the direction of the particle momentum. In the layered reconstruction framework, the position of the $Cluster^{2D}$ is regarded as the reconstructed position of centre of gravity. And $Cluster^{2D}$s will also provide the timestamp, which is related to the hit time of the particle, for the layers they belong to. For the position and time correction in this work, the layered correction is applied

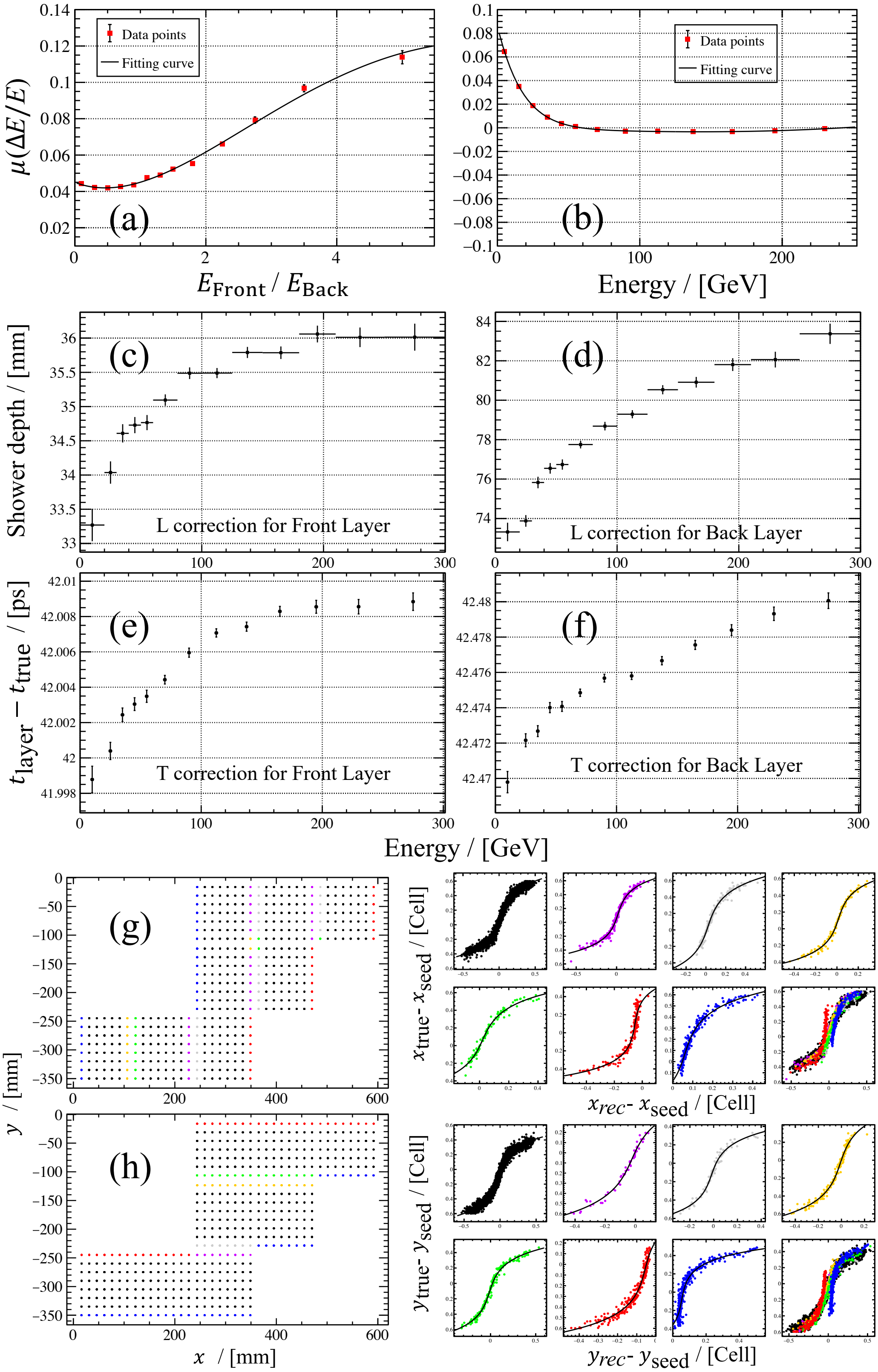

Fig. 3. (a, b): The energy correction. Here, ΔE is the difference between the true energy and the reconstructed energy, E is the true energy, and μ represents the mean value which is derived from the Gaussian fitting. (c, d): The L correction, where the shower depth is measured from the front surface of the ECAL. (e, f): The time correction points, where t_{true} is the true time of the particle at the front face of the ECAL. (g, h): The S correction.

343 to $Cluster^{2D}$s firstly, followed by the utilization of the cor-

344 rected information from $Cluster^{2D}$s to calculate the infor-

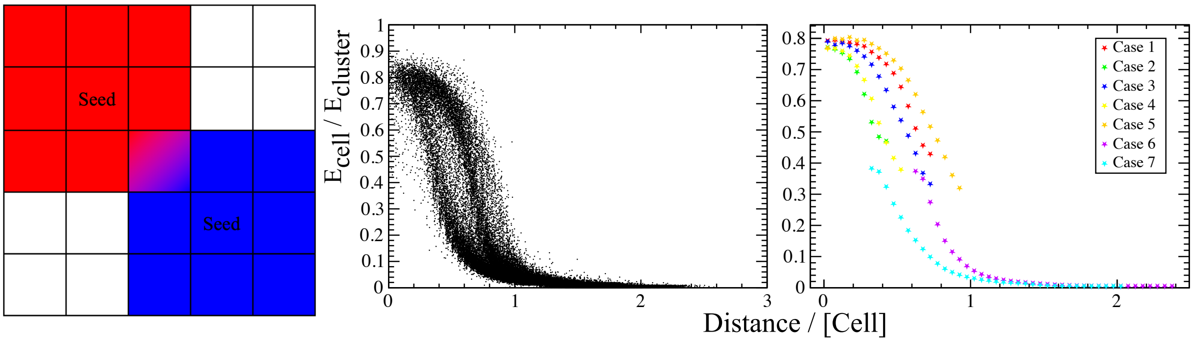

(a) (b)

Fig. 4. (a): Two overlapping clusters shared the same cell. (b): The transverse shower profile, where the y axis is the fraction of the energy of the $Cell^{2D}$s to the energy of the $Cluster^{2D}$s, and the x axis is the distance between the centre of the $Cell^{2D}$s and the centre of the $Cluster^{2D}$s.

mation of $Cluster^{3D}$s.

The purpose of the position correction is to correct the reconstructed position of the $Cluster^{2D}$ as accurately as possible to the centre of gravity of the energy deposited by the particles in each layer.

For the $Cluster^{2D}$, the x/y position information is derived from the energy-weighted positions of the $Cell^{2D}$s. Based on the model mentioned in Ref. [33], we define Δr_{rec} as the position of $Cluster^{2D}$ minus the position of $Seed^{2D}$, and Δr_{true} as the position of the true transversal energy barycentre minus the position of $Seed^{2D}$, in each layer. This work explores the relationship between Δr_{rec} and Δr_{true}. As shown in Fig. 3g and Fig. 3h, the shape of this relationship is like an S, so we also call the process of correcting the x/y coordinates "S correction". And S shape is affected by where the $Seed^{2D}$ is located. When the $Seed^{2D}$ is positioned at the boundaries of the region, the introduction of varying cell size of $Cell^{2D}$ and the presence of installation gaps will have an impact on the S shape. This results in a different S shape for $Cluster^{2D}$s locating at the boundary of the region compared to those inside the region, as also illustrated in Fig. 3g and Fig. 3h.

The z coordinate of the gravity center of the deposition energy is also usually used to evaluate the depth of the shower. Due to the typically small granularity and thick layers of ECAL in the longitudinal direction, directly using the z coordinate information of the $Cell^{2D}$ to reconstruct the z coordinate of the gravity center of the deposition energy in each layer would introduce substantial uncertainty. Therefore, the reconstruction of the z coordinate is typically performed based on the energy of the incident particles. As shown in Fig. 3c and Fig. 3d, the shower depth (Difference between the z coordinate of the shower and the z coordinate of the front face of the module) is logarithmically related to the incident particle energy due to the pair production of electrons dominated the energy deposition[34]. This is the rationale behind the term "L correction" for this correction step. By leveraging this correlation, we are able to deduce the z coordinate of the $Cluster^{2D}$ based on the energy of the incoming particle.

For the $Cluster^{2D}$s, the positions obtained by the above position correction are also projected onto the front surface of ECAL, and then will be used in the subsequent steps to calculate the position information of the $Cluster^{3D}$s.

In this work, the timestamp of the $Seed^{2D}$s are used as the timestamp for $Cluster^{2D}$s in the preliminary study. The purpose of time correction is to determine the time difference between the timestamps of the $Cluster^{2D}$ in each layer and the moment when the particle reaches a specific reference plane. This time difference is employed to correct the timestamp of the $Cluster^{2D}$ to the accurate time on a designated reference plane. And the front surface of ECAL is used as the reference plane for time correction in this work. Through research, this time difference is related to the energy of the incident particle, and the results of the correction are shown in Fig. 3e and Fig. 3f. Furthermore, if there is a rotation of the module, it will result in a longitudinal positional difference of $Cell^{2D}$s at different transverse positions on the same layer. This leads to a time difference for particles reaching different $Seed^{2D}$s on the same layer. Hence, it needs to compensate for this time difference based on the longitudinal position difference of $Seed^{2D}$s by following:

$$t'_{Seed^{2D}} = (t_{Seed^{2D}} + \frac{z_{Seed^{2D}} - z_{layer}}{v_z}), \tag{3}$$

where $t'_{Seed^{2D}}$ represents the compensated time of the $Seed^{2D}$, and v_z represents the velocity of the particle along the direction of the beam pipe.

After obtaining the corrected position and time information of $Cluster^{2D}$s, the time and position information of $Cluster^{3D}$s are obtained by weighting the time or position information of $Cluster^{2D}$s as follows:

$$V = r\ or\ t,$$
$$W_i(V) = \frac{1}{Res_i(V)^2},$$
$$V_{Cluster^{3D}} = \frac{\sum_{i=1}^{n}(V_{Cluster_i^{2D}} \times W_i(V))}{\sum_{i=1}^{n} W_i(V)}, \quad (4)$$

where the r represents the position, t represents the time, i represents the layer number and Res_i represents resolution of r or t in layer i, which are shown in Fig. 6b and Fig. 6c.

3. Splitting of overlapping clusters

When there is an overlap of two $Cluster^{3D}$s in an event, as depicted in Fig. 4a, it becomes necessary to conduct energy splitting on the shared $Cell^{2D}$s to ensure accurate reconstruction of the energy and position of the $Cluster^{3D}$s. In the layered reconstruction framework, the energy splitting of the overlapping $Cluster^{3D}$s is carried out at the $Cluster^{2D}$ level. The general logic of the algorithm is as follows: first, determine if the two $Cluster^{3D}$s share any $Cell^{2D}$s. If they do, distribute the energy of the shared $Cell^{2D}$s between the respective $Cluster^{2D}$s. Upon completing the energy splitting of $Cell^{2D}$s, reevaluate the information of $Cluster^{2D}$s based on the updated energy of $Cell^{2D}$s and remake necessary corrections.

Currently, the energy splitting is determined by the transverse shower profile obtained from MC truth information. This work provides a layered description of the transverse shower profile at the $Cell^{2D}$ level. As shown in Fig. 4b, the transverse shower profile is represented with the distance of $Cell^{2D}$s from $Cluster^{2D}$s on the x axis, and the energy fraction of $Cell^{2D}$s relative to $Cluster^{2D}$s on the y axis.

When a $Cell^{2D}$ is shared by two $Cluster^{2D}$s, the distribution of $Cell^{2D}$ energy to each $Cluster^{2D}$ is evaluated by two steps. Firstly, the energy fraction of the shared $Cell^{2D}$ corresponding to each $Cluster^{2D}$ is calculated based on the distance between the $Cell^{2D}$ and the $Cluster^{2D}$s, as depicted in Fig. 4b. Secondly, the estimated energy from each of the two $Cluster^{2D}$s to the $Cell^{2D}$ is computed by the fraction established in the first step and the energy of the $Cluster^{2D}$s. At this juncture, the total estimated energy from the two $Cluster^{2D}$s to the shared $Cell^{2D}$ exceeding the energy of the shared $Cell^{2D}$. The energy of the shared $Cell^{2D}$ is then distributed between the two $Cluster^{2D}$s using the aforementioned calculated estimated energy as the weighting factor. Subsequently, the energy and position of the $Cluster^{2D}$ are recalculated, and the aforementioned procedures are iterated. Upon the stabilization of the splitting weights of the shared $Cell^{2D}$ for two $Cluster^{2D}$s, this iterative process completes and finalizes the energy splitting of the shared $Cell^{2D}$.

The precision of the energy fraction contributed by $Cell^{2D}$s to each $Cluster^{2D}$ heavily relies on the accuracy of the transverse shower profile. As depicted in Fig. 4b, even when the distances between $Cell^{2D}$s and their respective $Cluster^{2D}$s are identical, the energy contribution from $Cell^{2D}$s to $Cluster^{2D}$s can vary significantly, and even displaying multiple peaks, particularly around distances of approximately 0.5 [Cell]. So, it is essential to categorize the data points in the left plot of Fig. 4b to achieve narrower fraction ranges corresponding to the same distance within a single category, as well as a singular peak in the energy fraction.

The classification method used in this work is in table 1 and the classification result is shown in the right plot of the Fig. 4b. Firstly, whether this $Cell^{2D}$ is a $Seed^{2D}$ should be determined. This is because the random scattering direction of the initial electron pairs affects which $Cell^{2D}$ near the hit point has the opportunity to receive more energy deposition. And a $Cell^{2D}$ deposited the maximum energy is constructed as a $Seed^{2D}$ in reconstruction process. Additionally, due to the shape of the readout unit ($Cell^{2D}$) not being a circle, the position of the hit point relative to the edges or corners of the $Seed^{2D}$ also affects the energy fraction of the $Seed^{2D}$ when the distance to the hit point is the same. Finally, the position of the hit point and the $Cell^{2D}$s relative to the $Seed^{2D}$ in the positive or negative direction of the particle's transverse momentum also affects the energy fraction, and this positional relationship can be described as being relatively close to or far from the beam pipe in LHCb. In practical operations, the hit position of particles in each layer is substituted by the position of $Cluster^{2D}$s.

C. Merged π^0 reconstruction

When two photons produced by π^0 cannot be reconstructed individually as two $Cluster^{3D}$s due to the proximity of the hit points, this π^0 is referred to as merged π^0. This section will describe how to reconstruct the potential sub-$Cluster^{3D}$ pair, which is considered to be the candidates of the photon pair from merged π^0, from a directly reconstructed $Cluster^{3D}$. Then, the sub-$Cluster^{3D}$ pair is used to reconstruct merged π^0. The workflow chart for merged π^0 reconstruction is shown in Fig. 5b. The following subsection will focus on the algorithms associated with the first and last steps in the workflow chart that have not appeared in single-photon reconstruction.

1. Searching the second $Seed^{2D}$ in $Cluster^{2D}$s

During the reconstruction process, a merged π^0 denotes its generated photon pair being reconstructed as one $Cluster^{3D}$ in the ECAL. And this indicates that the energy deposition from the π^0 only produces one local maximum energy $Cell^{3D}$. For the unlayered reconstruction framework in some experiments [35, 36], where layered readout information is lacking, it is a common practice to select one of the non-Seeded cells in the cluster with the highest energy cell as the second seed. Then, a new cluster is constructed around the second seed as the centre. After splitting the energy of the shared cells between the new cluster and the original cluster, the overlapping clusters are referred to as sub-cluster pair of the original cluster.

In fact, as shown in Fig. 5a, a merged π^0 does not necessarily result in "merged" $Cluster^{2D}$ in each layer. It is a

Table 1. The classification of transverse shower profile.

Case	Cell type	Hit position relative to Seed	Cell relative to Seed
1	Seed	1: In the positive direction of p_{T}; 2: Near the edges of the Seed	/
2	Seed	1: In the negative direction of p_{T}; 2: Near the edges of the Seed	/
3	Seed	1: In the positive direction of p_{T}; 2: Near the corner of the Seed	/
4	Seed	1: In the negative direction of p_{T}; 2: Near the corner of the Seed	/
5	Seed	Near the corner closest to the direction of p_{T} of the Seed	/
6	Cell	/	In the positive direction of p_{T}
7	Cell	/	In the negative direction of p_{T}

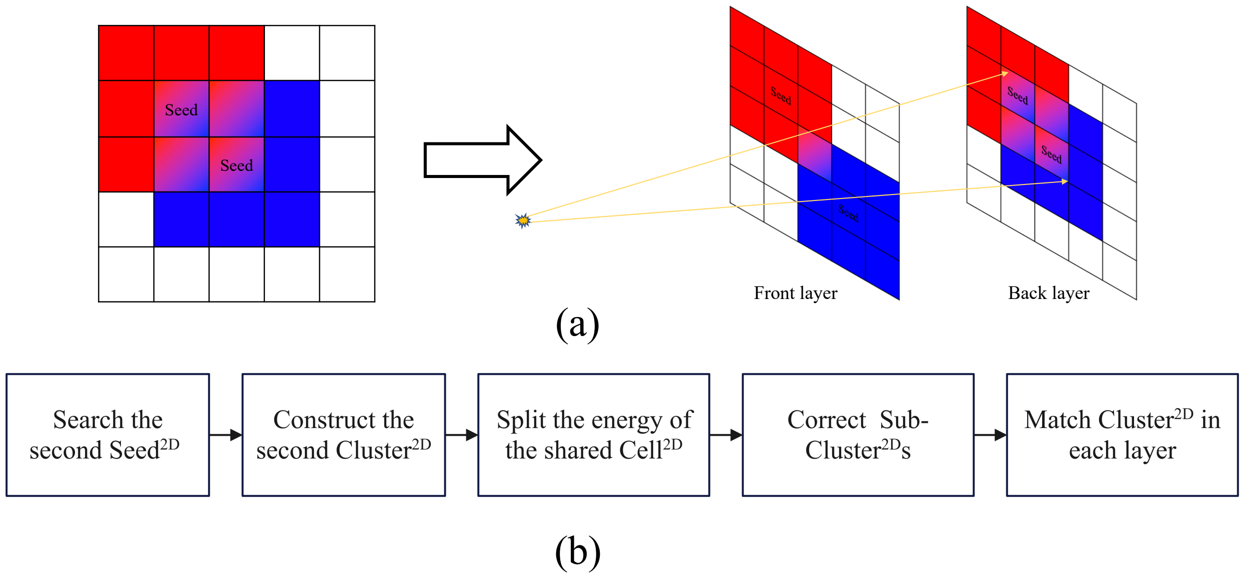

Fig. 5. (a): A possible $Cell^{3D}$s response and $Cell^{2D}$s response in each layer of a longitudinal segmented ECAL of a merged π^0. (b): Reconstruction flow chart for merged π^0.

well-established fact that, according to the cell energy splitting algorithm described above, the success rate of splitting increases as the number of cells shared by two clusters decreases.

Furthermore, it would be unjust to solely base the selection of the second $Seed^{2D}$ on the energy of $Cell^{2D}$s. Because the energy of $Cell^{2D}$s are also related to the distance from the hit point of photon. When one of the photons resulting from the decay of a π^0 has much higher energy than the other photon, in non-$Seed^{2D}$ $Cell^{2D}$s, the $Cell^{2D}$ closer to the higher-energy photon may have higher energy than the $Cell^{2D}$ closest to the lower-energy photon. Solely focusing on the energy of $Cell^{2D}$ may result in misidentification of the second $Seed^{2D}$.

Hence, motivated by the aforementioned reasons, the layered reconstruction framework described in this work involves a two-step process for identifying the second $Seed^{2D}$, aiming to enhance the accuracy of splitting $Cluster^{2D}$ and ultimately improve the efficiency of π^0 reconstruction.

The first step is to search the $Cell^{2D}$, except for the $Seed^{2D}$, with the highest energy of E' in $Cluster^{2D}$ as the $Cell^{2D'}$. The definition of E' can be found in the following equation:

$$E' = \frac{E(Cell^{2D})}{Frc}, \tag{5}$$

where the Frc is estimated ratio of the $Cell^{2D}$ and obtained by the relationship shown in Fig. 4b. The second step is to search whether there is any energy local maximum $Cell^{2D}$ other than $Seed^{2D}$ in the neighbouring $Cell^{2D}$s of the $Cell^{2D'}$ found in the first step. If there is, then the $Cell^{2D}$ with this energy local maximum is taken as the second $Seed^{2D}$, otherwise the $Cell^{2D'}$ is taken as the second $Seed^{2D}$. Subsequently, the second $Seed^{2D}$ is used to construct a new $Cluster^{2D}$ and the energy splitting for shared $Cell^{2D}$ and correction for $Cluster^{2D}$ will be done as detailed in previous sections.

2. *$Cluster^{2D}$ matching*

After completing the preliminary algorithm, there is sub-$Cluster^{2D}$ pair obtained in each layer. The algorithm described in this section aims to match the sub-$Cluster^{2D}$s in different layers, and finally obtain two sub-$Cluster^{3D}$s. The sub-$Cluster^{3D}$ pair is regard as the photons generated by merged π^0. The matching of $Cluster^{2D}$ on different lay-

ers will directly affect the correctness of the reconstruction of the final sub-$Cluster^{3D}$. The utilization of the multi-dimensional information from different readout layers facilitates more accurate $Cluster^{2D}$ matching.

At first, the energy of sub-$Cluster^{2D}$s in each layer is used for pre-matching. Since the ratio of deposition energy in each layer is related to the energy of the incident particles[25], unreasonable matches can be filtered out based on the energy ratios between the $Cluster^{2D}$s and the energy of the $Cluster^{3D}$ as Fig. 2b. For example, in the case of a dual-layer ECAL, the energy of the $Cluster^{2D}$s in the front layer is used to calculate the energy of the $Cluster^{2D}$s in the other layers, and if the energy of the $Cluster^{2D}$s in the other layers exceeds the calculated value by 3σ, the pre-matching is considered as a failure, and the matching result is filtered out.

If there is more than one $Cluster^{2D}$s in a certain layer pre-matched with the front layer, the final match is made based on the positional relationship. First, the $Cluster^{2D}$ in the front layer is connected with the initial vertex (usually the zero point). The connection line is extended and projected to the those layers, and the closest pre-matched $Cluster^{2D}$s to the projection point are matched with the front layer $Cluster^{2D}$ to complete the matching and get the sub-$Cluster^{3D}$.

Finally, in order to avoid resolved π^0 being reconstructed in a merged model, $Seed^{2D}$s in all layers of sub-$Cluster^{3D}$ need to be checked whether they are included in a direct reconstruction $Cluster^{3D}$. If so, the current process of merged π^0 reconstruction will be terminated and a new process will start by skipping to the next directly reconstructed $Cluster^{3D}$.

IV. PERFORMANCE

In the context of the LHCb experiment, a Phase-II Upgrade (LHCb Upgrade II) has been proposed[37]. Scheduled for installation at the beginning of LHC Run 5 around 2036, the LHCb Upgrade II aims to enhance the experiment's capabilities for exploring the frontiers of particle physics. The PicoCal is designed with a longitudinal layered ECAL structure. The Shashlik calorimeter structure [38, 39] will be retained in the outer region of the PicoCal, while the Spaghetti calorimeter (SpaCal) [40, 41] will be employed in the central region. The GAGG crystal, known for its great radiation resistance, high light yield, and excellent time response performance[42–47], will be introduced as a sensitive material into the most central region with the highest radiation dose. Reduced detector occupancy will be achieved by designing and using modules with smaller Molière radius to achieve smaller readout cell sizes in the internal regions with the highest detector occupancy. The detailed layout is provided in table 2.

In this section, based on the above layout, a series of single-photon and π^0 samples are used to demonstrate the performance of the layer reconstruction algorithm in this framework. Additionally, the unlayered reconstruction algorithm[33] employed in Run 1/2 of LHCb is introduced for comparison. To ensure fairness, the unlayered reconstruction algorithm remains consistent with layered reconstruction algorithm in cluster correction, overlapping cluster splitting, and other steps, except for the utilization of layered information.

A. Single photon performance

The single photon samples utilized in this section are generated and simulated using the "Hybrid MC" simulation framework [48], which is built upon the GEANT4 Monte Carlo package [49]. The performance of the layered reconstruction algorithm in this framework will be demonstrated in terms of energy, position, and time resolution.

Table 2. Modules in 2023 baseline setup of PicoCal.

Region	Type	Absorber/Crystal	Cell size $[\mathrm{cm}^2]$	R_M [mm]	Layers
1	Shashlik	Lead/Polystyrene	12×12	35.0	2
2	Shashlik	Lead/Polystyrene	6×6	35.0	2
3	Shashlik	Lead/Polystyrene	4×4	35.0	2
4-7	SpaCal	Lead/Polystyrene	3×3	29.5	2
8-11	SpaCal	Tungsten/GAGG	1.5×1.5	14.5	2

1. *Energy resolution*

The Fig. 6a illustrates the energy resolution versus the incident energy. And the relationship is described by the following equation:

$$\sigma(E)/E = \frac{a}{\sqrt{E}} \oplus b, \tag{6}$$

where a represents the statistical fluctuations of the readout signal (e.g., photoelectrons), b represents constant term errors due to uncertainties in the calibration and correction, as well as inhomogeneities in the active material, and $\oplus$ represents the sum of squares. The energy resolution and bias as a function of energy illustrate the stability of the layered reconstruction framework. And, as illustrated in Fig. 7, layered reconstruction algorithm demonstrates better energy resolution for the particles with large incident angles. However, due to the forward detector design and the layout of the PicoCal[31], there are fewer single-photon events with large incident angles. Therefore, this improvement is not significantly reflected in the energy resolution as a function of the incident particle energy.

2. *Position resolution*

The position resolution is a critical parameter of the ECAL and, to some extent, is also equivalent to angular resolution. The position resolution is illustrated in Fig. 6b and d, where the $Front$ and $Back$ represent the front and back layer, r represent the position. As particles undergo showering and

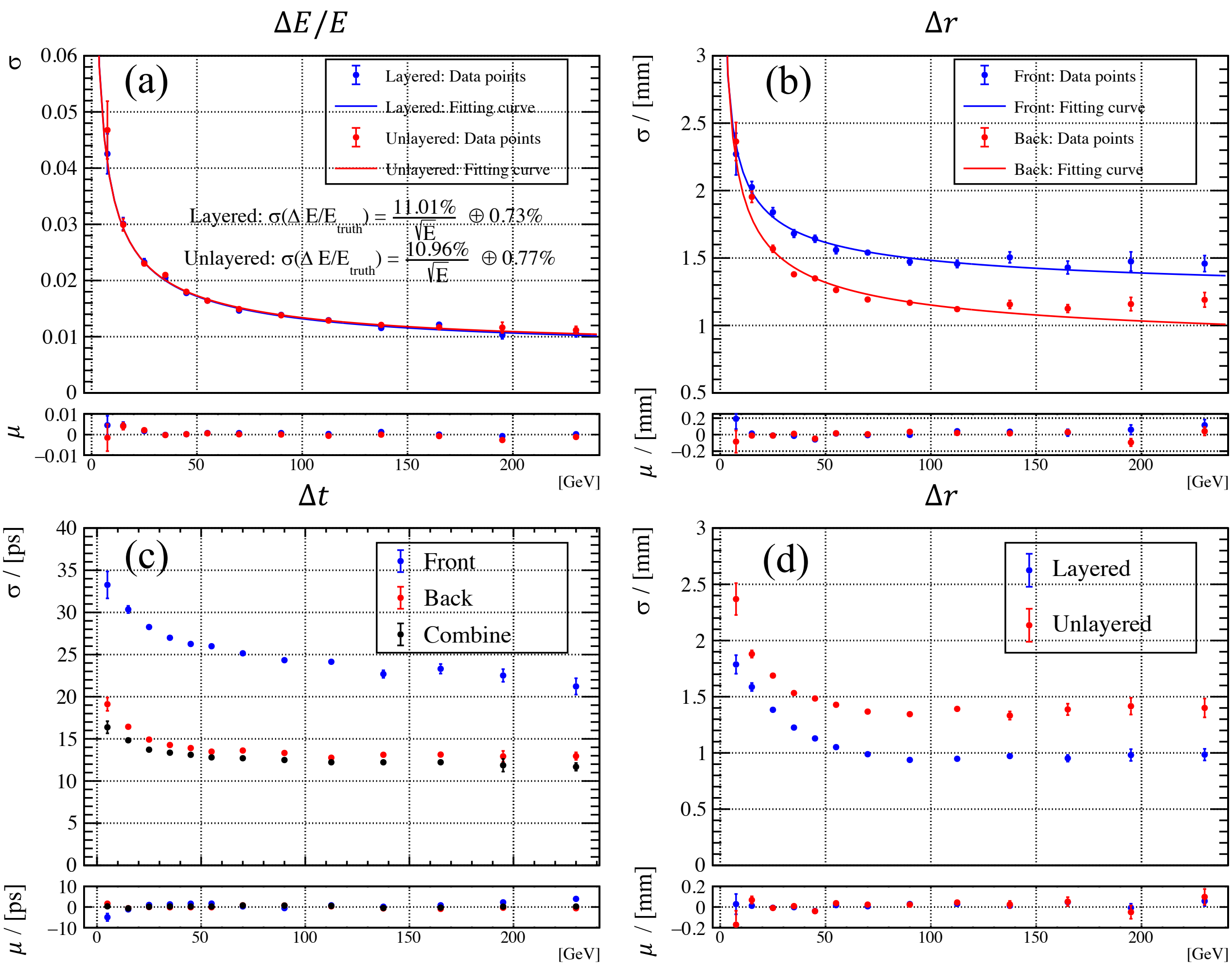

Fig. 6. The resolution and bias relative to the true value in regions 4-7. σ and μ are derived from the Gaussian fitting, where σ represents the standard deviation (used to denote the resolution) and μ is the mean value (used to denote the bias). (a): The energy resolution and bias, where ΔE is the difference between the true energy and the reconstructed energy, and E is the true energy. (b): The position resolution and bias of front and back layers, where Δr is the difference between the true position and the reconstructed position. (c): The time resolution and bias, where Δt is the difference between the true time and the reconstructed time. (d): The position resolution and bias, where Δr is the difference between the true position and the reconstructed position.

deposit energy along their momentum direction, the development stages of the shower will change, as well as the readout layer it is on. However, the tendency for the reconstructed $Cluster^{2D}$'s raw position relative to the true position will vary between different layers. Essentially, if we only have energy-weighted position information of $Cell^{2D}$s located in different layers, the raw position will spread out in the transverse plane due to the different tendency. Consequently, utilizing an unlayered reconstruction algorithm and an overall correction parameters for reconstructing the transverse position will lead to a degradation of the position resolution due to this spreading effect. In contrast, the reconstruction in this work effectively resolves the previously mentioned issue and improves the positional resolution, as illustrated in Fig. 6d. This enhancement results in an improvement of approximately 0.5 mm in the high-energy region, representing a 33% increase compared to the unlayered reconstruction algorithm.

3. *Time resolution*

Time information is essential for event reconstruction and data analysis in the high luminosity environment. Within the layered reconstruction framework, time information can be provided in the form of $Cluster^{3D}$ or along the longitudinal direction using $Cluster^{2D}$, as depicted in Fig. 6c. The integration of layered time information will provide new analytical perspectives for upcoming physical investigations. And ongoing research is also focusing on exploring the application of time information in reconstruction, correction, and analyses.

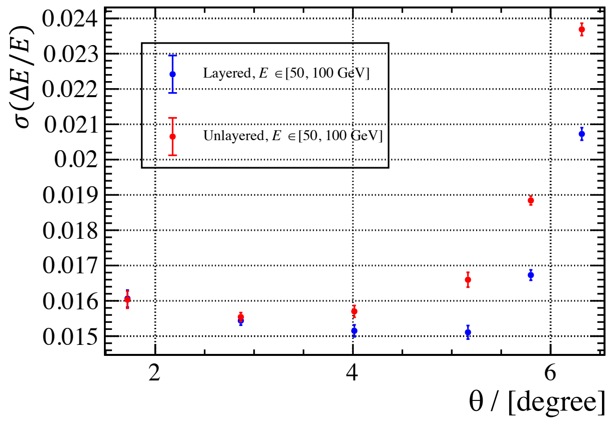

Fig. 7. The energy resolution versus angle θ in regions 4-7. Here, θ is the angle between the particle's motion direction and the beam direction. ΔE represents the difference between the true energy and the reconstructed energy, and the E represents the true energy. σ is the standard deviation and derived from the Gaussian fitting.

B. π^0 reconstruction performance

In this section, around 30000 signal π^0 events from $B^0 \to \pi^+\pi^-\pi^0$ have been generated by the generation part of Gauss[50], with the requirement that all final-state photons from π^0 should to be contained within the acceptance region of the ECAL. The transverse momentum distribution of the π^0s is shown in Fig. 8a. Those samples are used as a benchmark to test the contribution of the layered reconstruction algorithm in this framework to the reconstruction performance of π^0 particles. The matched $M(\gamma\gamma)$ distribution which compare with the unlayered reconstruction algorithm is shown in Fig. 8b and Fig. 8c. And the reconstruction efficiency of π^0 based on layered reconstruction framework is shown in Fig. 8f. The efficiency comparison between the layered and unlayered reconstruction algorithms is shown in Fig. 8d and Fig. 8e, with resolved and merged modes presented separately.

As shown in Fig. 8d, as expected, utilizing the layered reconstruction algorithm in this framework improves the ability to split overlapping $Cluster^{3D}$ s, leading to a 10% increase in the efficiency of reconstructing merged π^0. And the improvement of position resolution of single photon contributes to the resolution improvement of π^0 mass distribution as shown in Fig. 8b and Fig. 8c.

V. COMPUTATION

This framework allows for task splitting according to events, enabling different events to be deployed as separate tasks. Based on this framework, we evaluated the runtime of $Cluster^{3D}$ reconstruction under the LHCb PicoCal at a center-of-mass energy of 14 TeV and an instantaneous luminosity of 1.5×10^{34} cm^{-2}s^{-1}. The framework is deployed in a cluster CPU with CPU $Intel(R)\ Xeon(R)\ Platinum$ 9242 CPU @ 2.30 GHz for each task. Since the events are independent of each other in this framework, we only consider the time consumption of the reconstruction for each individual event. For comparison, we also introduced the unlayered reconstruction algorithm used in LHCb, with the results shown in Fig. 9. Compared to the unlayered reconstruction algorithm, the layered reconstruction algorithm does not significantly increase computation time.

In a CPU cluster, scalability is a critical consideration. Within this framework, an event is defined as the smallest unit of a cluster task. This approach facilitates efficient task management and resource allocation. By increasing the number of computing nodes, the number of events processed in parallel can be increased, thereby reducing the overall runtime of the tasks. And utilizing more powerful CPUs in each computing node can enhance the computation speed for event reconstruction.

In the reconstruction process of each event, the time complexity of each step in the flowchart shown in Fig. 2d is presented in table 3. Here, n_1 represents the number of the $Cell^{2D}$s, n_2 represents the number of the $Cell^{3D}$s, n_3 represents the number of the $Seed^{3D}$s, and n_4 represents the number of the $Cluster^{3D}$s. Taking parallelism within an event into account, the structure of these processes in this framework has been designed for future deployment on nodes with parallel computing capabilities, such as GPUs or FPGAs. This establishes a solid foundation for the future deployment and acceleration of these algorithms on GPU clusters and FPGA platforms.

VI. CONCLUSION

As depicted in Fig. 1, this work has accomplished the development of a software framework for longitudinal segmented ECAL event reconstruction. Moreover, the layered reconstruction algorithm has been devised within this framework for $Cluster^{3D}$s and merged π^0. In this framework, it not only furnishes the general direction, arrival time, and energy of the particle candidates by the $Cluster^{3D}$ format, but also provides position, timestamp, and energy deposition in each layer by the $Cluster^{2D}$ format. The information from the $Cluster^{2D}$s can not only be used to filter out unreasonable $Cluster^{3D}$s during reconstruction, but also provide new perspectives in physics analysis.

To achieve a more refined correction of the $Cluster^{3D}$ information, this work leveraged the advantages of a layered reconstruction framework to provide layered information and designed a layered correction method and process. In terms of energy correction, compared to solely using the $Cluster^{3D}$ energy for correction, this work further utilized the energy ratios of the $Cluster^{2D}$ in each layer for correction, aiming to better compensate for the longitudinal variation in sampling fraction of the ECAL. For the correction of time and position information, this work first corrected the corresponding information of the $Cluster^{2D}$s, and then weighted the corrected $Cluster^{2D}$ information based on the resolution of the corre-

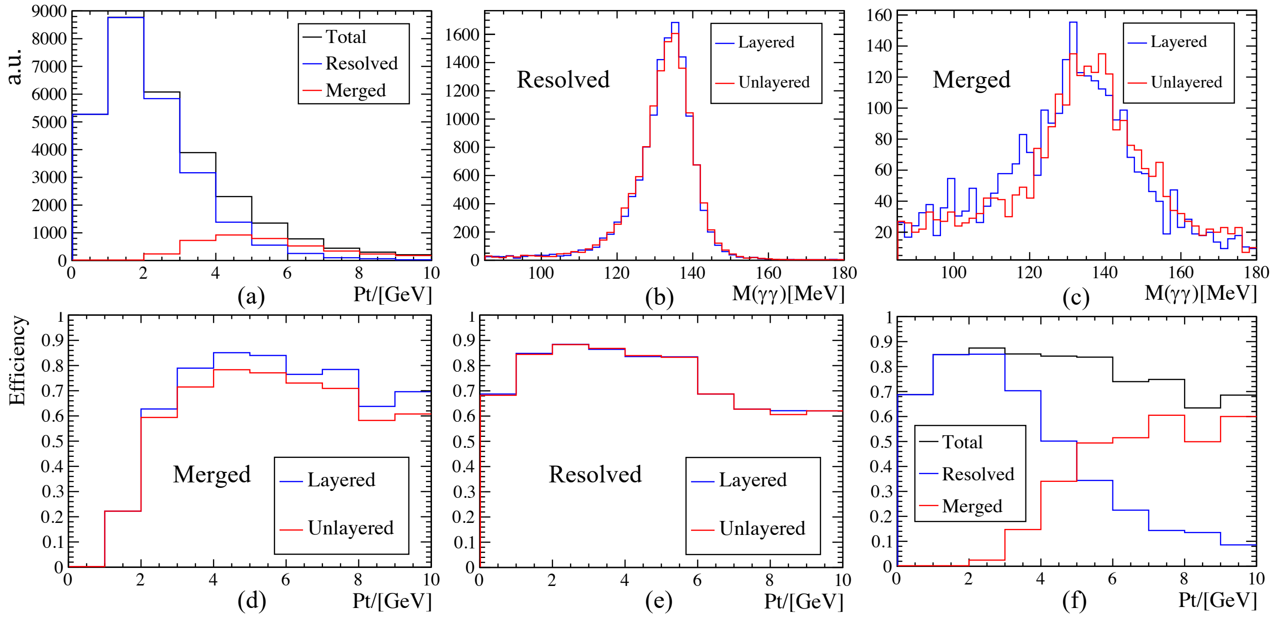

Fig. 8. (a): The transverse momentum distribution of π^0 from $B^0 \to \pi^+\pi^-\pi^0$. (b): The distribution of $M(\gamma\gamma)$ of matched candidates in the resolved model in the SpaCal region. (c): The distribution of $M(\gamma\gamma)$ of matched candidates in the merged model in the SpaCal region. (d): The reconstruction efficiency of merged π^0 from $B^0 \to \pi^+\pi^-\pi^0$. (e): The reconstruction efficiency of resolved π^0 from $B^0 \to \pi^+\pi^-\pi^0$. (f): The total reconstruction efficiency of π^0 from $B^0 \to \pi^+\pi^-\pi^0$ in layered reconstruction framework.

Table 3. The time complexity.

Algorithm	Time complexity
Construct $Cell^{3D}$s	$O(n_1)$
Search $Seed^{3D}$s	$O(n_2)$
Construct $Cluster^{3D}$s	$O(n_3)$
Split overlapping $Cluster^{3D}$s	$O(n_4^2)$
Search $Seed^{2D}$s/Construct $Cluster^{2D}$s	$O(n_4)$
Correct $Cluster^{3D}$s	$O(n_4)$

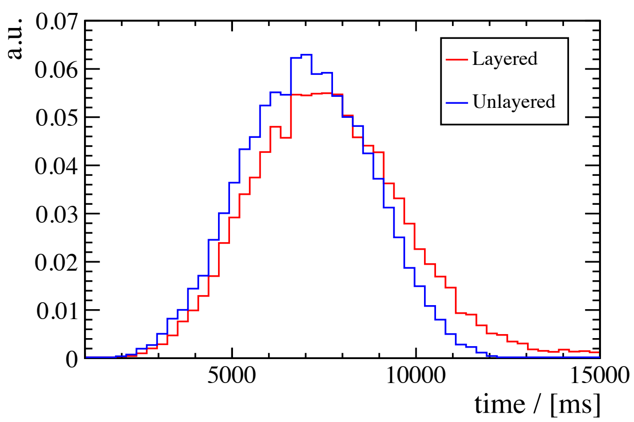

Fig. 9. The time consumption distribution for each event.

sponding information in each layer. The weighted result is used as the corrected information for the $Cluster^{3D}$. Moreover, this work delves into the transverse shower profile and systematically elucidates the relationship between distance and energy ratio between $Cell^{2D}$ s and $Cluster^{2D}$. This information provides more precise prior knowledge for the splitting of the overlapping $Cluster^{3D}$s.

Finally, the performance of the framework was validated using the PicoCal in LHCb Upgrade II. The results show that the layered reconstruction algorithm in this framework significantly improves the position resolution of the single-photon and the energy resolution of the particles at large incident angles compared to the unlayered reconstruction algorithm. For example, in regions 4-7 of the specified setup, the position resolution has enhanced from approximately 1.4 mm to 0.9 mm in the high-energy region. Additionally, the energy resolution has improved by about 10% at large incident angles. Furthermore, the layered reconstruction algorithm enhances the splitting capability of overlapping clusters, leading to a further improvement in the efficiency of merged π^0 reconstruction. In the current version of the algorithms, it can increase the reconstruction efficiency of merged π^0 by approx-

imately 10% at the SpaCal in the mentioned setup.

Furthermore, this work provides a suitable software platform for future research on layered ECAL. Since it incorporates comprehensive data structures and application programming interfaces (APIs), along with straightforward configuration and execution procedures. This feature allows for convenient secondary development leveraging the framework to substitute and validate new algorithms. And this also facilitating investigations into ECAL-related physics. In future work, we will continue to explore various facets utilizing the multi-dimensional information and scalability provided by this software framework. This includes delving into the application of deep learning in cluster splitting and cluster information correction, evaluating the performance of different cluster shapes, and scrutinizing the application of time information in cluster reconstruction, among others.

VII. ACKNOWLEDGMENTS

We would like to express our gratitude to Marco Pizzichemi, Loris Martinazzoli and Philipp Gerhard Roloff in LHCb ECAL Upgrade II R&D group for developing the simulation software and great suggestion that is really helpful in our work. Additionally, we extend our thanks to the developers and maintainers of the Gauss software in LHCb, which we used to generate events.

---

[1] X.Z. Yu, X.Y. Wang, W.H. Ma et al., Production and test of sPHENIX W/SciFiber electromagnetic calorimeter blocks in China. NUCL SCI TECH. 35, 145 (2024). https://doi.org/10.1007/s41365-024-01517-y

[2] J.Y. Zhu, Y.Z. Su, H.B. Yang et al., Design and prototyping of the readout electronics for the transition radiation detector in the high energy cosmic radiation detection facility. NUCL SCI TECH. 35, 82 (2024). https://doi.org/10.1007/s41365-024-01446-w

[3] J. Zhu, X.Y. Peng, S.Y. Luo, W.C. Xiao et al., Performance of the electromagnetic calorimeter module in the NICA-MPD based on Geant4. NUCLEAR TECHNIQUES. 46(12): 120202 (2023).

[4] S. Acharya et al., Performance of the ALICE Electromagnetic Calorimeter. JINST. **18** no.08, P08007 (2023). doi: 10.1088/1748-0221/18/08/P08007.

[5] Rolf Lindner, LHCb Particle Identification Enhancement Technical Design Report. CERN, Technical Report No. CERN-LHCC-2023-005, LHCB-TDR-024, Geneva (2023). doi: 10.17181/CERN.LAZM.F5OH. https://cds.cern.ch/record/2866493

[6] T. Boettcher, Direct photon production at LHCb. Nuclear Physics A. **982**, 251-254 (2019). doi: 10.1016/j.nuclphysa.2018.10.046. https://www.sciencedirect.com/science/article/pii/S0375947418303270

[7] The LHCb Collaboration, LHCb Detector Performance. International Journal of Modern Physics A **30** (07), 1530022 (2015). doi: 10.1142/S0217751X15300227. https://doi.org/10.1142/S0217751X15300227

[8] C. Abellán Beteta, A. Alfonso Albero, Y. Amhis et al., Calibration and performance of the LHCb calorimeters in Run 1 and 2 at the LHC. 2020, Report Number: LHCb-DP-2020-001. https://cds.cern.ch/record/2729028

[9] The LHCb Collaboration, Observation of Photon Polarization in the $b \to s\gamma$ Transition. Phys. Rev. Lett. **112** (16), 161801 (2014). doi: 10.1103/PhysRevLett.112.161801. https://link.aps.org/doi/10.1103/PhysRevLett.112.161801

[10] The LHCb Collaboration, First experimental study of photon polarization in radiative B_s^0 decays. Physical review letters, 118(2), 021801. https://doi.org/10.1103/PhysRevLett.118.021801

[11] The LHCb Collaboration, Measurement of CP Violation in the Decay $B^+ \to K^+\pi^0$. Phys. Rev. Lett. **126** (9), 091802 (2021). doi: 10.1103/PhysRevLett.126.091802. https://link.aps.org/doi/10.1103/PhysRevLett.126.091802

[12] The LHCb Collaboration, Search for time-dependent CP violation in $D^0 \to \pi^+\pi^-\pi^0$ decays. Phys. Rev. Lett. 133, 101803 (2024). doi: 10.1103/PhysRevLett.133.101803.

[13] The LHCb Collaboration, Test of Lepton Universality with $B^0 \to K_*^0\ell^+\ell^-$ Decays. Journal of High Energy Physics **2017**, 55 (2017). doi: 10.1007/JHEP08(2017)055. https://doi.org/10.1007/JHEP08(2017)055

[14] The LHCb Collaboration, Test of lepton universality in $b \to s\ell^+\ell^-$ decays. Phys. Rev. Lett. 131, 051803 (2023). doi: 10.1103/PhysRevLett.131.051803.

[15] The LHCb Collaboration, Search for the $B_s^0 \to \mu^+\mu^-\gamma$ decay. JHEP 2407, 101 (2024). doi: 10.1007/JHEP07(2024)101.

[16] The LHCb Collaboration, Expression of Interest for a Phase-II LHCb Upgrade: Opportunities in flavour physics, and beyond, in the HL-LHC era. CERN Technical Report, CERN-LHCC-2017-003, Geneva (2017). https://cds.cern.ch/record/2244311

[17] The LHCb Collaboration, Framework TDR for the LHCb Upgrade II: Opportunities in flavour physics, and beyond, in the HL-LHC era. CERN, Technical Report No. CERN-LHCC-2021-012, LHCB-TDR-023, Geneva (2021). https://cds.cern.ch/record/2776420

[18] The LHCb Collaboration, Physics case for an LHCb Upgrade II - Opportunities in flavour physics, and beyond, in the HL-LHC era. CERN, Technical Report No. LHCB-PUB-2018-009, CERN-LHCC-2018-027, LHCC-G-171, Geneva (2016). doi: 10.17181/CERN.QZRZ.R4S6. https://cds.cern.ch/record/2636441

[19] I. Efthymiopoulos et al., LHCb Upgrades and operation at $10^{34} cm^{-2} s^{-1}$ luminosity – A first study. (2018). https://cds.cern.ch/record/2319258

[20] L.M. Huhta, Physics program and performance of the ALICE Forward Calorimeter upgrade (FoCal). Proceedings of the 31st International Workshop on Deep Inelastic Scattering (DIS2024). (2024). https://cds.cern.ch/record/2910362

[21] F. Orlandi, Upgrade of the CMS Barrel Electromagnetic Calorimeter for the LHC Phase-2. CERN, report number CMS-CR-2024-133, Geneva (2024). https://cds.cern.ch/

record/2908787

[22] The ATLAS Collaboration, Technical Design Report: A High-Granularity Timing Detector for the ATLAS Phase-II Upgrade. CERN, ATLAS-TDR-031. Geneva (2020). https://cds.cern.ch/record/2719855

[23] Q.Y. Shou, Y.G. Ma, S. Zhang, et al., Properties of QCD matter: a review of selected results from ALICE experiment. NUCL SCI TECH. 35, 219 (2024). https://doi.org/10.1007/s41365-024-01583-2

[24] J.H. Chen, X. Dong, X.H. He, et al., Properties of the QCD matter: review of selected results from the relativistic heavy ion collider beam energy scan (RHIC BES) program. NUCL SCI TECH. 35, 214 (2024). https://doi.org/10.1007/s41365-024-01591-2

[25] M. Livan and R. Wigmans, Calorimetry for Collider Physics, an Introduction, 1st ed. (2019). http://lib.ugent.be/catalog/ebk01:4100000008707558

[26] The CMS Collaboration, Performance of electron reconstruction and selection with the CMS detector in proton-proton collisions at $\sqrt{s}$ = 8 TeV. JINST, vol. 10, p. P06005, 2015. doi: 10.1088/1748-0221/10/06/P06005. https://cds.cern.ch/record/1988091

[27] The CMS Collaboration, Electron and photon reconstruction and identification with the CMS experiment at the CERN LHC. JINST, vol. 16, no. 05, p. P05014 (2021). doi:10.1088/1748-0221/16/05/P05014. https://cds.cern.ch/record/2747266

[28] The CMS Collaboration, Performance of photon reconstruction and identification with the CMS detector in proton-proton collisions at $\sqrt{s}$= 8 TeV. JINST, vol. 10, p. P08010 (2015). doi: 10.1088/1748-0221/10/08/P08010. https://cds.cern.ch/record/1988093

[29] S. Nair, Simulation studies of π^0, η and ω meson reconstruction performance in pp collisions at $\sqrt{s}$ = 14 TeV in Forward Calorimeter(FoCal). Indian Inst. Tech. Indore, 2023. https://cds.cern.ch/record/2860262

[30] Sergei Kholodenko, LHCb ECAL UII working group, LHCb ECAL upgrade II. PoS **PANIC2021**, 100 (2022). doi: 10.22323/1.380.0100. https://cds.cern.ch/record/2836693.

[31] The LHCb Collaboration, LHCb Upgrade II Scoping Document. CERN. CERN-LHCC-2024-010, LHCB-TDR-026. Geneva. 2024. https://cds.cern.ch/record/2903094

[32] V. Breton, N. Brun, and P. Perret, A clustering algorithm for the LHCb electromagnetic calorimeter using a cellular automaton. CERN. LHCb-2001-123. Geneva (2001). https://cds.cern.ch/record/681262

[33] O. Deschamps, F. P. Machefert, M. H. Schune, G. Pakhlova, and I. Belyaev, Photon and neutral pion reconstruction. CERN-LHCb-2003-091 (2003).

[34] C. Grupen and B. Shwartz, *Particle Detectors*, 2nd edition, Cambridge Monographs on Particle Physics. Nuclear Physics and Cosmology (Cambridge University Press, Cambridge, 2008).

[35] F. P. Machefert, P. Robbe, M. H. Schune, O. Deschamps, A. Robert, $B^0 \to \pi^+\pi^-\pi^0$ reconstruction with the re-optimized LHCb detector. CERN, Technical Report No. LHCb-2003-077, Geneva (2003). https://cds.cern.ch/record/691636

[36] H. Terrier, I. Belyaev, Particle identification with LHCb calorimeters. CERN (2003). url: https://cds.cern.ch/record/691743

[37] The LHCb Collaboration, The LHCb Detector at the LHC. *Journal of Instrumentation* **3**, S08005 (2008). doi: 10.1088/1748-0221/3/08/S08005. https://dx.doi.org/10.1088/1748-0221/3/08/S08005

[38] S. Barsuk, A. Golutvin, V. Kochetkov, I. Korolko, S. Malyshev, V. Mayatski, V. Yu Rusinov, A. Soldatov, and E. Tarkovski, Design and construction of electromagnetic calorimeter for LHCb experiment. CERN Technical Report, LHCb-2000-043, Geneva (2000). https://cds.cern.ch/record/691508

[39] The LHCb Collaboration, LHCb calorimeters: Technical Design Report. CERN, Technical Design Report. LHCb, Geneva (2000). https://cds.cern.ch/record/494264

[40] P. Jenni, P. Sonderegger, H. P. Paar, and R. Wigmans, The high resolution spaghetti hadron calorimeter: proposal. CERN Technical Report, NIKHEF-H-87-7, Geneva (1987). https://cds.cern.ch/record/181281

[41] L. An, E. Auffray, F. Betti et al., Performance of a spaghetti calorimeter prototype with tungsten absorber and garnet crystal fibres. *Nuclear Instruments and Methods in Physics Research Section A: Accelerators, Spectrometers, Detectors and Associated Equipment* **1045**, 167629 (2023), ISSN: 0168-9002. doi: 10.1016/j.nima.2022.167629. https://www.sciencedirect.com/science/article/pii/S0168900222009214

[42] V. Alenkov, O. Buzanov, G. Dosovitskiy et al., Irradiation studies of a multi-doped Gd3Al2Ga3O12 scintillator. Nucl. Instrum. Methods Phys. Res. A. 916, 226-229 (2019). https://doi.org/10.1016/j.nima.2018.11.101

[43] K. Kamada et al., Composition Engineering in Cerium-Doped (Lu,Gd)3(Ga,Al)5O12 Single-Crystal Scintillators. Crystal Growth & Design. vol. 11, no. 10, pp. 4484-4490 (2011). doi: 10.1021/cg200694a. https://doi.org/10.1021/cg200694a

[44] M. Nikl et al., Defect Engineering in Ce-Doped Aluminum Garnet Single Crystal Scintillators. Crystal Growth & Design. vol. 14, no. 9, pp. 4827-4833 (2014). doi: 10.1021/cg501005s. https://doi.org/10.1021/cg501005s

[45] M.T. Lucchini et al., Effect of Mg^{2+} ions co-doping on timing performance and radiation tolerance of Cerium doped $Gd_3Al_2Ga_3O_{12}$ crystals. Nuclear Instruments and Methods in Physics Research Section A: Accelerators, Spectrometers, Detectors and Associated Equipment. vol. 816, pp. 176-183 (2016). https://doi.org/10.1016/j.nima.2016.02.004

[46] L. Martinazzoli et al., Scintillation properties and timing performance of state-of-the-art $Gd_3Al_2Ga_3O_{12}$ single crystals. Nuclear Instruments and Methods in Physics Research Section A: Accelerators, Spectrometers, Detectors and Associated Equipment. vol. 1000, pp. 165231 (2021). https://doi.org/10.1016/j.nima.2021.165231

[47] M. T. Lucchini, K. Pauwels, K. Blazek, S. Ochesanu, E. Auffray, Radiation Tolerance of LuAG:Ce and YAG:Ce Crystals Under High Levels of Gamma- and Proton-Irradiation. IEEE Transactions on Nuclear Science. **63** (2), 586-590 (2016). doi: 10.1109/TNS.2015.2493347.

[48] M. Pizzichemi, L. Martinazzoli, Hybrid-MC. (2024). https://gitlab.cern.ch/spacal-rd/spacal-simulation

[49] S. Agostinelli, J. Allison, K. Amako, et al., Geant4—a simulation toolkit. Nuclear Instruments and Methods in Physics Research Section A: Accelerators, Spectrometers, Detectors and Associated Equipment. **506** (3),

250-303 (2003). doi: 10.1016/S0168-9002(03)01368-8. https://www.sciencedirect.com/science/article/pii/S0168900203013688

[50] The LHCb Collaboration, The LHCb Simulation Application, Gauss: Design, Evolution and Experience. Journal of Physics: Conference Series. **331**, 032023 (2011). doi: 10.1088/1742-6596/331/3/032023. url: https://dx.doi.org/10.1088/1742-6596/331/3/032023